Spin polarization and quantum-statistical effects in ultracold ionizing collisions

C. Orzel,* M. Walhout,† U. Sterr,‡ P. S. Julienne, and S. L. Rolston
National Institute of Standards and Technology, PHY A167, Gaithersburg, Maryland 20899
(Received 20 July 1998)

We have measured ultracold ionizing collision rates for three bosonic (^{132}Xe, ^{134}Xe, and ^{136}Xe) and two fermionic (^{129}Xe and ^{131}Xe) isotopes of xenon in the $6s[3/2]_2$ metastable state, for both spin-polarized and unpolarized samples. For unpolarized samples at temperatures above the *p*-wave centrifugal barrier (~ 39 μK), we find that collision rates for all isotopes are identical. Quantum-statistical effects forbid *s*-wave collisions for spin-polarized fermions, giving rise to significant differences between bosonic and fermionic isotopes below the *p*-wave barrier. We present a technique for measuring collision rates at temperatures below 1 μK, and find that the ratio of polarized to unpolarized collision rates for fermions decreases by a factor of 2 at low temperatures, while the ratio for bosons increases by 50%. We find no evidence of an overall reduction in the collision rate for spin-polarized samples, as has been observed in metastable helium. These results are explained using a simple theoretical model of transmission and quantum reflection off long-range interatomic potentials. [S1050-2947(99)02802-4]

PACS number(s): 34.80.Nz, 32.80.Pj, 34.50.Fa

I. INTRODUCTION

The study of ultracold atomic collisions has generated much theoretical and experimental interest in recent years [1], and understanding these collision processes has proven to be crucial to many areas of physics, from atomic clocks [2] to the pursuit of Bose-Einstein condensation (BEC) [3–5] in dilute atomic vapors. Collisions have been studied in laser-cooled samples of most alkali atoms, leading to improved measurements of atomic lifetimes and scattering lengths through photoassociation spectroscopy [6], and providing the impetus for the development of new theoretical methods for cold collisions [7], collisions in light fields [8], and new calculations of interatomic potentials [9].

Rare-gas (RG) metastable systems, such as the Xe* system studied here, have proven to be exceptionally useful in the study of cold collision physics. For colliding rare-gas metastables in the $np^5(n+1)s$ state (where $n=2$, 3, 4, 5 for Ne, Ar, Kr, and Xe) or He in the 2^3S state, the Penning and associative ionization reactions

$$\begin{aligned} &\text{Penning:} \quad \mathrm{RG^*} + \mathrm{RG^*} \rightarrow \mathrm{RG} + \mathrm{RG}^+ + e^-, \\ &\text{Associative:} \quad \mathrm{RG^*} + \mathrm{RG^*} \rightarrow \mathrm{RG_2}^+ + e^- \end{aligned} \tag{1}$$

provide a direct and easily detectable measure of collision processes. These ionizing collisions are the dominant collisional processes in most metastable atom traps, and we can monitor the rate of collisions by monitoring the rate of ion production. Rare-gas metastable systems have been used to study collisions in optical lattices [10,11], to study the modification of collision rates by the application of laser light [12–15], and in time-resolved studies of the collision process [16]. Understanding these collisions is also of critical importance to those attempting to achieve BEC in metastable atom systems [17–19].

In this paper, we report on a study of these collisions which makes use of another important feature of the metastable xenon system. There are nine stable isotopes of xenon, all of which may be laser cooled and trapped in the $6s[3/2]_2$ metastable state; both bosons (even mass number) and fermions (odd mass number) are available. We use xenon atoms from a magneto-optical trap (MOT) to compare collision rates between various isotopes, and employ a ballistic expansion technique to study collisions at very low energies where we observe large differences between bosonic and fermionic isotopes due to quantum-statistical effects. A study comparing two isotopes of krypton has previously observed a $\sim 10\%$ difference between collision rates for fermions and bosons due to this effect for collisions at temperatures near the *p*-wave centrifugal barrier [20]; here, we present measurements at temperatures below 1 μK and find a factor of 3 difference between the two rates.

We measure the rate of collisions between cold atoms by monitoring the rate of ion production, which has the form [12]

$$R_i = \alpha_i N + \frac{\beta}{2} \int n^2(\mathbf{r}) d^3 r, \tag{2}$$

where N is the total number of cold atoms, and $n(\mathbf{r})$ is the atomic density distribution in the sample. The term in α_i describes ionizing collisions between cold atoms and atoms of background gas, and β describes the loss rate from the sample due to ionizing collisions between atoms in the sample. The factor of $\frac{1}{2}$ accounts for the fact that two atoms are lost for each ion produced in a collision. We measure these rate coefficients β for our samples.

Section II of this paper will explain the origin and low-temperature behavior of these β coefficients, and show how quantum-statistical effects change these rates. In Sec. III we explain the ''expansion cooling'' effect which we exploit to

*Permanent address: Chemical Physics Program, University of Maryland, College Park, MD 20742-2431.
†Permanent address: Physics Department, Calvin College, Grand Rapids, MI 49546.
‡Permanent address: Physikalisch-Technische Bundesanstalt, D-38116 Braunschweig, Germany.

measure collision rates at sub-μK temperatures. Sections IV and V present our measurements of β for five different isotopes, first for unpolarized samples of atoms at temperatures above the *p*-wave centrifugal barrier, and then comparing spin-polarized and unpolarized samples at temperatures below 1 μK for both bosonic and fermionic isotopes.

II. THEORY

A. Quantum threshold behavior

Collisions between atoms at ultracold temperatures ($T<1$ mK) are qualitatively different than collisions at ''normal'' temperatures. At ultracold temperatures, the de Broglie wavelength associated with the atomic motion becomes longer than the typical scale of the interatomic potential, and semiclassical descriptions of the collision process break down. Only a very few partial waves contribute to the collision, and quantum threshold effects dominate the behavior of those channels.

A full description of quantum threshold behavior in ultracold collisions is beyond the scope of this paper. Here we present a sketch of the basic threshold effects applicable to the xenon system, following the approach of Ref. [7].

Two colliding metastable atoms experience a long-range interatomic potential of the form

$$U_{mol}(R)=-\frac{C_6}{R^6}+\frac{\hbar^2 l(l+1)}{2\mu R^2}, \tag{3}$$

where R is the internuclear separation, and μ the reduced mass of the system. The term in C_6 represents the attractive van der Waals potential between the atoms [21], and the term in $l(l+1)$ produces the centrifugal barrier associated with the partial wave having angular momentum l.

For atoms colliding in the initial state γ (where γ represents the properly symmetrized wave function describing the internal $|J,m_J\rangle$ quantum states of the two colliding atoms), we can calculate a collisional cross section σ_l for each partial wave l (with associated projections $|m|\leq l$), given by

$$\sigma_l(E,\gamma\rightarrow\gamma')=\frac{\pi}{k^2}\sum_m\sum_{l',m'}|T_{l,m,l',m'}(E,\gamma\rightarrow\gamma')|^2, \tag{4}$$

where $k=(2\mu E)^{1/2}$ is the wave vector associated with a collision energy E, and the sum over l' and m' is over the angular momentum states associated with the final state. The matrix $\mathbf{T}$ is related to the scattering matrix $\mathbf{S}$ by $\mathbf{T}=\mathbf{1}-\mathbf{S}$, and describes the probability of scattering from the initial quantum state γ to a particular final state γ'. The total scattering cross section for a given partial wave,

$$\sigma_l^{(\mathrm{tot})}(E,\gamma)=\sum_{\gamma'}\sigma_l(E,\gamma\rightarrow\gamma'), \tag{5}$$

is obtained by summing over all possible final states γ'.

For sufficiently strong exothermic inelastic processes, like those involved in Penning ionization of Xe* [22], the sum over exit channel states γ' is dominated by only a few terms, as any atoms which penetrate the centrifugal barrier are lost through these exothermic inelastic channels with essentially unit probability. In this limit, Eq. (5) reduces to an expression for the *ionization* cross section,

$$\sigma_l^{(\mathrm{ion})}(E,\gamma)=\frac{\pi}{k^2}(2l+1)P_T(E,l), \tag{6}$$

summing the $\sigma_l(E,\gamma\rightarrow\gamma')$ for all exit channels γ' involving ionization. $P_T(E,l)$ is the probability of transmission through the centrifugal barrier for partial wave l. For the *s* wave, which has no centrifugal barrier, $P_T(E,0)$ is determined by the probability of quantum reflection off the long-range C_6/R^6 potential, due to the mismatch between the long asymptotic de Broglie wave and the rapidly varying wave in the region of small internuclear separation.

The analysis of Ref. [7] shows that, for such an exothermic inelastic process, the cross sections vary as k^{2l-1} for $k\rightarrow 0$. Thus, for *p*- and *d*-wave collisions at very low energies, the cross sections vary as k and k^3, respectively. For the *s* wave, however, the cross section diverges as $\sigma_0^{(\mathrm{ion})}(E)\propto 1/k$. Thus the inelastic scattering cross sections at very low temperatures become quite large, and can dominate over elastic collision processes (the *s*-wave elastic cross section approaches a constant).

The physically relevant quantity in experiments using trapped atoms is the collisional rate coefficient

$$\beta_l(T,\gamma)=2\langle\sigma_l^{(\mathrm{ion})}(E,\gamma)v\rangle_T, \tag{7}$$

where the brackets denote an average over the relative collisional velocities v described by the thermal distribution at temperature T. Since $v=\hbar k/\mu$, this cancels the divergence of σ_0, and we find $\beta_0\rightarrow$const for the *s* wave as $T\rightarrow 0$. As the temperature decreases, the higher angular momentum states begin to drop out ($\beta_l\rightarrow 0$ for $l\geq 1$), while the *s*-wave collisional rate coefficient approaches a constant value, and dominates the collision process for very low T. The factor of 2 in Eq. (7) is due to the fact that β is defined as a collisional *loss* rate, and two atoms are lost for each ionization event.

In this limit of strong inelastic processes, we can calculate the ionization rate coefficient using only long-range interatomic potentials. This is a significant simplification, as the long-range potentials have been calculated, while the details of the short-range potentials are not known for this system. For strong enough ionization, we can reduce the problem to a one-dimensional system in which the potential is set to a (negative) constant at short range, and allowed to extend to $R=-\infty$. This is equivalent to the assumption of Eq. (6), that all atoms penetrating to short range are lost through the strong inelastic (ionization) channels. The cross sections and collisional rate coefficients are then determined only by the probability $P_T(E,l)$ of transmission through the long-range potential. Previous experiments [12] and calculations using complex potentials to model the ionization process [23] suggest that this simple model should accurately describe Penning ionizing collisions in the Xe* system.

We use a theoretical value of $C_6=5810e^2a_o^5$ (where $a_o=0.529\times10^{-10}$ m is the Bohr radius, and $e=1.6\times10^{-19}$ C is the electron charge) for Xe*+Xe* [24] for the interatomic potential at long range [$U(R)=-C_6/R^6$ for $R\geq R_{\mathrm{cut}}$], and set the potential to a constant value of $U(R_{\mathrm{cut}})$ for $R<R_{\mathrm{cut}}$, extending to $R=-\infty$. We calculate the prob-

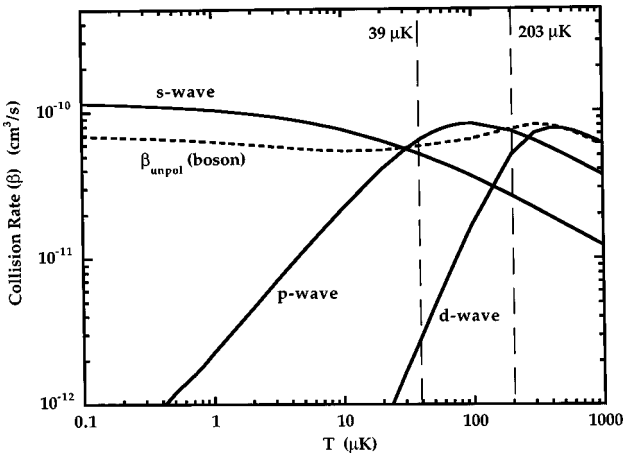

FIG. 1. Collisional rate coefficients β as a function of temperature for s, p, and d ($l=0,1,2$) partial waves. Vertical lines show the locations of the centrifugal barriers for the p-wave (39 μK) and d-wave (203 μK). The broken line is the total collisional rate calculated for an unpolarized sample of bosons.

abilities $P_T(E,l)$ using these model potentials for various partial waves by numerically solving the Schrödinger equation in one dimension. These probabilities are found to be independent of the radius $R_{\rm cut}$ at which the potential is assigned to a constant, for $R_{\rm cut} \leqslant 25a_o$. The rate coefficients calculated from these probabilities and Eqs. (6) and (7) for the s, p, and d waves are shown in Fig. 1.

For these potentials, we find centrifugal barrier heights of 39 μK for the p wave and 203 μK for the d wave. At temperatures below these values, the contribution of the associated partial waves decreases dramatically. At typical MOT temperatures of ~ 100 μK, partial waves higher than the d wave do not contribute significantly to the collision. At ~ 10 μK (well below the p wave barrier), the s wave accounts for more than 80% of the total collision rate coefficient for an unpolarized sample of bosons.

These theoretical rates depend only on the long-range C_6/R^6 potentials, which are insensitive to small changes in properties such as the atomic mass, which may significantly alter the short-range interatomic potentials. Under these assumptions, we expect to find a universal collisional rate for ionizing Xe* collisions, independent of isotope. From this simple model, we calculate a rate coefficient of $\beta_{\rm tot} \approx 6.5 \times 10^{-11}$ cm^3/s at $T \sim 100$ μK. We have measured a rate coefficient of $\beta_{\rm tot} = 6(2) \times 10^{-11}$ cm^3/s [25] in a previous experiment [12]. The good agreement between our experimental data and this simple model justifies the simplifying assumption of Eq. (6), that atoms which penetrate the centrifugal barriers will ionize with essentially unit probability.

These rate coefficients are also in good agreement with complex-potential calculations [23]. The calculated rate coefficients remain essentially constant over a wide range of complex potential parameters in this model, though it is possible to obtain significant changes in the rate coefficients if the scattering length becomes very large. While the scattering length is sensitive to small changes in the atomic mass, such large scattering lengths occur only over narrow ranges of the potential parameters. With the small number of isotopes, and the discrete mass values available, it is unlikely that such a large scattering length will occur in a real sample. Thus, we expect there to be very little variation in the β coefficients for the various isotopes of xenon, though it is possible that some isotope will have a rate coefficient which is significantly different from those for the other isotopes.

B. Quantum-statistical effects

The quantum threshold laws form the basis for understanding the ultracold collision process, but this basic picture must be modified to take into account the quantum-statistical character of the atoms. Atoms in the same $|J,m_J\rangle$ [26] internal states are identical particles, and the scattering wave functions must be modified to preserve this indistinguishability, and obey the proper symmetrization relations for bosons or fermions. As a consequence of this symmetrization, identical bosons may collide only in even-l partial waves (s wave, d wave, etc.), while fermions may collide only in odd-l partial waves (p wave, f wave, etc.).

For a pair of atoms A and B, with internal states given by $|J,m_J\rangle$, we can write a scattering channel wave function

$$\Phi_l = Y_{lm}(\theta,\phi)|J,m_J\rangle_A|J',m_J'\rangle_B, \tag{8}$$

where the spherical harmonic $Y_{lm}(\theta,\phi)$ describes the partial wave l. For particles with spin, however, we must consider the properly symmetrized combinations of the state described by Eq. (8) and the corresponding state upon exchange of nuclei A and B. These are given by

$$\begin{aligned}\psi_l &= \Phi_l \pm \Phi_l^{(\rm ex)} \\ &= \frac{1}{\sqrt{2+2\delta_{J,J'}\delta_{m_J,m_J'}}}\,[Y_{lm}(\theta,\phi)|J,m_J\rangle_A|J',m_J'\rangle_B \\ &\quad \pm (-1)^l Y_{lm}(\theta,\phi)|J',m_J'\rangle_A|J,m_J\rangle_B]\end{aligned} \tag{9}$$

where $1/\sqrt{2+2\delta_{J,J'}\delta_{m_J,m_J'}}$ ensures proper normalization and $(-1)^l$ is the result of the exchange operation on the $Y_{lm}(\theta,\phi)$.

For bosons, we must take the symmetric combination $\psi_l^{(\rm sym)} = \Phi_l + \Phi_l^{(ex)}$. When the internal atomic quantum states are identical, Eq. (9) becomes

$$\psi_l^{(\rm boson)} = Y_{lm}(\theta,\phi)|J,m_J\rangle_A|J,m_J\rangle_B \quad \text{for even } l. \tag{10}$$

The wave functions are identically zero for odd partial waves, indicating that bosons in the same internal quantum states may collide only through channels with even collisional angular momentum. For fermions, we must take the antisymmetric combination $\psi_l^{(\rm anti)} = \Phi_l - \Phi_l^{(\rm ex)}$, and find that the scattering wave function vanishes identically for *even* values of l, and thus only odd partial waves are allowed in collisions between fermions with identical internal states.

These quantum statistical effects must be taken into account when determining the collision rate expected from a sample of xenon in a MOT. Atoms in different internal states are distinguishable particles, and may collide in any partial waves; atoms in the same internal state may only collide in those partial waves which are allowed for their spin species. We can calculate the rate coefficients $\beta_l(T,\gamma)$ using the for-

mulas of Sec. II A, and then sum these rate coefficients over the distribution of m_J levels, as in Ref. [20].

For an unpolarized sample of atoms having total internal angular momentum J, the probability of a collision between two atoms in the same m_J magnetic sublevel is $1/(2J+1)^2$. Making the simplifying assumption that $\beta_l(T,\gamma)$ are independent of the internal states (γ) of the atoms, the total collision rate coefficient for an unpolarized sample of bosons is

$$\beta_{\text{unpol}}^{(\text{boson})}(T)=\frac{2J+1}{(2J+1)^2}\beta_{\text{even}}(T)+\frac{(2J+1)2J}{(2J+1)^2}\frac{1}{2}(\beta_{\text{even}}(T)+\beta_{\text{odd}}(T)), \tag{11}$$

where β_{even} and β_{odd} are the sums of the rate coefficients β_l for even and odd partial waves, respectively. The first term describes collisions between atoms in the same m_J sublevels, the second describes collisions between atoms with different internal states. The dotted line in Fig. 1 shows $\beta_{\text{unpol}}^{(\text{boson})}(T)$ for our simple model.

For a fully spin-polarized sample of bosons, where all the atoms are in the same m_J state, the total rate coefficient reduces to

$$\beta_{\text{pol}}^{(\text{boson})}(T)=\beta_{\text{even}}(T). \tag{12}$$

The ratio of polarized to unpolarized rates is then

$$\eta^{(\text{boson})}(T)=\frac{\beta_{\text{pol}}^{(\text{boson})}(T)}{\beta_{\text{unpol}}^{(\text{boson})}(T)}=\frac{(2J+1)\beta_{\text{even}}(T)}{(J+1)\beta_{\text{even}}(T)+J\beta_{\text{odd}}(T)}. \tag{13}$$

As $T\rightarrow 0$, we know from Sec. II A that the collisional rate coefficient for the s wave approaches a constant value, while those for all other partial waves vanish. Thus $\beta_{\text{even}}\rightarrow$const, while $\beta_{\text{odd}}\rightarrow 0$, and approaches

$$\eta^{(\text{boson})}(T)=\frac{\beta_{\text{pol}}^{(\text{boson})}(T)}{\beta_{\text{unpol}}^{(\text{boson})}(T)}\rightarrow\frac{2J+1}{J+1}, \tag{14}$$

which gives a value of $\frac{5}{3}$ for the $J=2$ $6s[3/2]_2$ state in Xe*. We can perform similar calculations for arbitrary distributions of m_J states.

For a sample of fermions, the roles of even and odd partial waves are switched, and the ratio [Eq. (13)] becomes

$$\eta^{(\text{fermion})}(T)=\frac{\beta_{\text{pol}}^{(\text{fermion})}(T)}{\beta_{\text{unpol}}^{(\text{fermion})}(T)}=\frac{(2J+1)\beta_{\text{odd}}(T)}{(J+1)\beta_{\text{odd}}(T)+J\beta_{\text{even}}(T)}. \tag{15}$$

In this case, as $T\rightarrow 0$, β_{odd} again goes to zero, and the ratio of polarized to unpolarized rates vanishes at low temperature. The only collision channel allowed at low T is the s wave, and polarized fermions are forbidden to collide in any even partial wave, leading to a dramatic reduction in the collision rate coefficient for polarized samples as $T\rightarrow 0$.

For sufficiently high temperatures, many partial waves will contribute to the collision, and $\beta_{\text{even}}\approx\beta_{\text{odd}}$. Then the ratio $\eta\rightarrow 1$ for high T, for both bosons and fermions.

C. Polarization and spin conservation

The preceding analysis has explicitly assumed that there is no dependence of the collision rate on the internal $|J,m_J\rangle$ states of the colliding atoms. This assumption is called into question, particularly for spin-polarized samples, by considering the role of spin in the ionizing collision process.

The Penning ionization reaction should conserve the total spin of the system, which places a strong limit on the ionization rate in a polarized sample. Spin conservation is calculated to have a dramatic effect in metastable triplet helium ($^4\text{He}(2^3S)$) [18]. Looking at the spins involved in the general Penning ionization reaction, for a spin-polarized sample,

$$\begin{array}{rccccccc} & \text{RG}^* & + & \text{RG}^* & \rightarrow & \text{RG} & + & \text{RG}^+ + e^-, \\ \text{Spin:} & s_a=1 & + & s_b=1 & | & s_a=0 & + & s_b=\tfrac{1}{2} + s_c=\tfrac{1}{2}, \\ \text{Total spin:} & & S_R=2 & & | & & & S_P=1, \end{array} \tag{16}$$

we see that the reactants have a total spin of $S_R=2$, while the maximum possible spin of the products is $S_P=1$. For the reaction to proceed, one of the electron spins must change its value, so the reaction is forbidden (to the degree that S is a good quantum number throughout the collision). Theoretically, this is predicted to suppress the Penning ionization rate for helium by a factor of 10^5 [18], with collisions occurring only due to a weak spin-spin dipole interaction, which makes the spin-flip possible. Measurements in a room-temperature rf discharge [27] show that the collision rate for spin-polarized He* is suppressed by at least an order of magnitude.

For heavier rare-gas metastables, the LS (Russell-Saunders) coupling scheme begins to break down, as the spin-orbit interaction becomes quite strong, and only the total angular momentum $\mathbf{J}=\mathbf{L}+\mathbf{S}$ is a good quantum number. Thus one might expect that this argument, which depends on conservation of $\mathbf{S}$, would break down for heavier atoms.

For the $|J=2,m_J=2\rangle$ ''stretched state'' (which is the state used for spin-polarized experiments), however, the

spin-conservation argument is still valid. The total angular momentum $J=2$ is obtained by coupling the $L=1$ state in the $5p^5$ core with the two $s=\frac{1}{2}$ spins of the unpaired $5p^5$ core electron and the $6s$ valence electron (total $S=1$). To obtain the maximum projection $|J=2, m_J=2\rangle$ state, both electron spins must be aligned with the orbital angular momentum of the core. For this fully aligned state (and the $|J=2, m_J=-2\rangle$ state), L and S are *effectively* good quantum numbers, and the argument of Ref. [18] should still hold. For any of the other m_J states, S is not a good quantum number, and ionization proceeds through the normal channels.

The difference between He* and other rare-gas metastables lies in the interactions which produce the spin-flip which makes Penning ionization possible. In helium, both core and valence electrons are in s states ($1s$ and $2s$, respectively), so the interatomic potentials are completely isotropic. In this case, the anisotropic interaction which changes the orientation of the electron spin is believed to be a weak spin-spin dipole potential, which gives a rate five orders of magnitude below the normal ionization rate.

For xenon (and, indeed, all rare-gas metastables other than He*), while the valence electron remains in an s state, the unpaired core electron is in a p state. The presence of this orbital angular momentum gives rise to interactions which depend on the relative orientations of the atoms (the $1/R^5$ quadrupole-quadrupole potential, for example), which can create energy differences between the Σ, Π, and Δ molecular potentials involved in the collisions.

When this occurs, the angular momenta of the colliding atoms will ''lock'' to the molecular axis defined in the collision, and the internal states of the atoms will adjust to keep the projection Ω of the total angular momentum $\mathcal{J}$ along that axis fixed. As the core reorients, the spin-orbit interaction induces a spin-flip, taking the system out of the $|J=2, m_J=2\rangle$ state (in the space-fixed frame) where ionizing collisions are forbidden, and into a state where ionization can proceed.

The effect of this mixing due to anisotropic interactions can be many times stronger than the spin-spin dipole relaxation which limits the suppression effect in He*. For sufficiently strong interactions, it is even possible for spin polarization to produce an *increase* in the collision rate coefficient [17]. Any change in $\beta(T)$ due to spin-conservation effects may be described theoretically by a simple extension of the model of Sec. II B.

III. EXPANSION COOLING

In order to best observe the effects described in Sec. II B, we must have samples at temperatures significantly below the p-wave centrifugal barrier of 39 μK, as seen in Fig. 1. This is well below the typical MOT operating temperature of ~ 100 μK, and while the necessary temperatures may be reached through sub-Doppler laser-cooling techniques, low temperatures are achieved at the cost of reducing the number of atoms in the sample, which reduces the experimental signal. Additionally, we wish to measure the collision rate over a wide range of temperatures, both above and below the p-wave barrier, which would be a rather time-consuming process if samples were prepared individually for each temperature point.

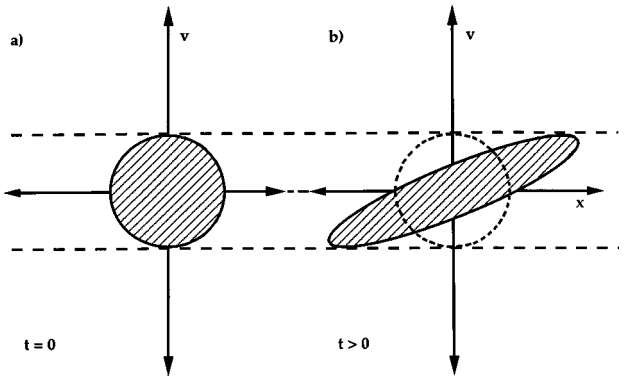

FIG. 2. Phase-space picture of the expansion cooling mechanism discussed in the text. The circle plotted in part (a) shows the rms widths of the spatial and velocity distributions of a trapped sample of atoms. After ballistically expanding for a time t, we find the narrower distribution of part (b), giving rise to a lower effective temperature for collisions. The dotted circle shows the size of the initial distribution.

For our measurements, we use a technique exploiting the correlations which develop between position and velocity in a ballistically expanding cloud of atoms. As the cloud expands, there is a monotonically decreasing *effective* temperature for interatomic collisions. Starting with a dense sample at normal MOT temperatures, we can use this technique to measure collision rates over two orders of magnitude in T in a single experiment.

This effect can be understood from a simple qualitative picture. We consider a small sample of atoms with a thermal distribution of velocities, allowed to expand ballistically. After the atom cloud has expanded significantly with respect to the initial size of the sample, there are strong correlations between position and velocity. Atoms with very different velocities will be widely separated from one another; atoms with similar velocities will be quite close to one another. This leads to an effective reduction in the temperature for collisions, as those atoms which are close enough to collide have very similar velocities, and hence very low *relative* velocities. It is this relative velocity which determines the collision properties described in Sec. II.

More quantitatively, we consider a sample of atoms in one dimension with a Gaussian distribution of initial positions with an rms width given by x_o, and a velocity distribution described by a temperature T_o and associated rms velocity width $v_o=\sqrt{k_B T_o/m}$ (where k_B is the Boltzmann constant). We can plot this distribution in phase space $(x/x_o, v/v_o)$, as a circle of unit radius representing the $1/\sqrt{e}$ points of the distribution. This is shown in Fig. 2(a). The full width of this distribution at any point x is given by

$$\Delta v = 2v_o \sqrt{1-\frac{x^2}{x_o^2}}. \tag{17}$$

After the cloud has expanded for a time t, we find the distribution shown in Fig. 2(b). The spatial extent of the cloud is increased due to the outward flight of the atoms, while the total velocity width of the distribution (shown by

the dashed lines) is unchanged during ballistic expansion. As the total number of atoms is conserved, the total area enclosed by the figure must remain constant. This leads to the narrowing of the distribution seen in Fig. 2(b).

The full width of this distribution is given by

$$\Delta v = \frac{2v_o}{\sqrt{1+\frac{v_o^2t^2}{x_o^2}}}\sqrt{1-\frac{x^2}{x_o^2\left(1+\frac{v_o^2t^2}{x_o^2}\right)}}$$

$$= 2v_{\rm eff}(t)\sqrt{1-\frac{x^2}{x_{\rm eff}(t)^2}}, \tag{18}$$

in analogy with Eq. (17). Here

$$x_{\rm eff}(t) = \sqrt{x_o^2\left(1+\frac{v_o^2t^2}{x_o^2}\right)} \tag{19}$$

is the spatial rms width of the cloud at time t, while

$$v_{\rm eff}(t) = \frac{v_o}{\sqrt{1+\frac{v_o^2t^2}{x_o^2}}} \tag{20}$$

is the effective rms velocity spread at any point in the sample at time t. Note that the velocity width of the sample *as a whole* is unchanged. This effective velocity width describes only the local distribution of velocities, which is the relevant quantity in discussions of collision processes.

From the effective velocity, we can extract an effective temperature

$$T_{\rm eff}(t) = \frac{T_o}{1+\frac{v_o^2t^2}{x_o^2}}, \tag{21}$$

and we see that it depends only on the initial width of the velocity distribution and the initial size of the sample. These are quantities which we directly measure in our experiments. We can thus measure the collision rate as a function of temperature by monitoring the collision rate as a function of time during the ballistic expansion of the cloud, and converting the expansion time t to the effective temperature $T_{\rm eff}$ using our measured values of x_o and T_o.

For a very long expansion, such that $v_o^2t^2 \gg x_o^2$, we see that

$$T_{\rm eff} \approx \frac{T_o}{\frac{v_o^2t^2}{x_o^2}} = \frac{m}{k_B}\frac{x_o^2}{t^2}, \tag{22}$$

since $T_o = mv_o^2/k_B$. The effective temperature reached in a given time t then depends only on the initial size of the atom cloud, and not on the initial temperature. To obtain the lowest possible effective temperature for a given expansion time t, it it necessary only to prepare as small a trap as possible. This allows us to start from a MOT at (relatively) high temperature with a large number of atoms at high density, and take full advantage of our dense trapped samples.

The expansion of the cloud is unaffected by collisions between the atoms, on the time scale of interest for our experiments. In the 40-ms duration of our measurement, we would expect 0.26 ionizing collisions per atom if the sample were held at the peak density of 10^{11} cm^{-3}. As the density drops by several orders of magnitude due to the expansion of the cloud, the actual number of collisions is far smaller, and the effect of these collisions on the expansion should be negligible. The effect of elastic collisions should be negligible as well, as the rate coefficients for elastic collisions are estimated to be slightly smaller those for ionizing collision at our initial temperature T_o, and will decrease as $\sqrt{T_{\rm eff}}$ [7], in addition to the decrease in density.

Typical experimental values of v_o are of order 6 cm/s, and rms trap sizes are ~ 100 μm, allowing us to reach effective temperatures as low as 0.1 μK after 40 ms of free expansion. The range of effective temperatures attainable is limited only by the loss of signal as the atoms fall under gravity, dropping out of the detection region. The present experiment represents the first use of this effect as a technique for studying low-temperature collision effects. This expansion cooling effect has previously been discussed in studies of atomic clocks [2].

IV. UNPOLARIZED COLLISION RATES

We measure the rate coefficients β by monitoring the rate of ion production from collisions between atoms in our trap, which has the form given in Eq. (2). If we assume a Gaussian density profile for our trap, the integral of Eq. (2) reduces to

$$R_i = \alpha_i N + \frac{\beta}{2^{5/2}} N n_o, \tag{23}$$

where n_o is the peak density in the trap. To obtain rate coefficients for unpolarized samples of various isotopes, we measure N and n_o directly by absorptive imaging of the MOT, and use these values to extract β for the various isotopes.

The contribution of the background collision term $\alpha_i N$ to the signal is quite small, as the gases which typically make up the background in our vacuum chamber have ionization potentials well above the 8 eV available in collisions with a Xe* metastable. Thus collisions between background gas atoms and trapped metastables, while they may lead to trap loss, are unlikely to produce an ion. Measurements of α_i [12] are consistent with $\alpha_i = 0$, with a maximum possible value on the order of 10^{-3} s^{-1}, which would give an ion count rate comparable to the background rate for our detection system with no MOT present. For all the measurements which follow, we assume $\alpha_i = 0$.

The apparatus for cooling and trapping metastable xenon is described in Ref. [28]. Repumping lasers for the odd isotopes (the even isotopes have no nuclear spin, no hyperfine structure, and need no repumping lasers) are provided by a second laser, to ensure efficient loading of the MOT for these isotopes. Using a low magnetic-field gradient ($B_g \sim 10$ mT/m) to make a large MOT, we typically load

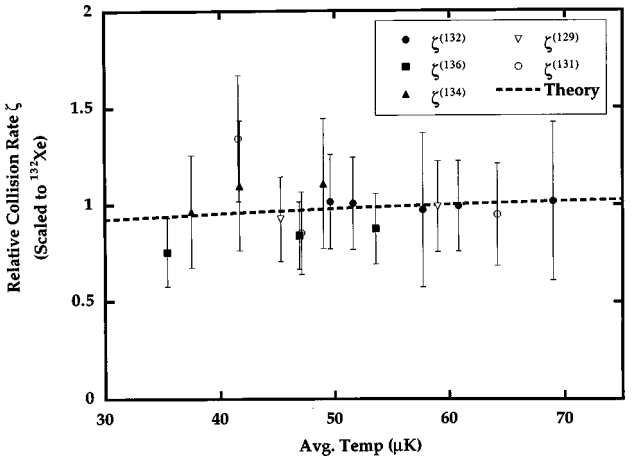

FIG. 3. Measured relative collisional rate coefficients ζ_{unpol} for unpolarized samples of three bosonic (^{132}Xe, ^{134}Xe, and ^{136}Xe) and two fermionic (^{129}Xe and ^{131}Xe) isotopes, scaled to the average rate for ^{132}Xe. Rates are measured after 4 ms of ballistic expansion, and T_{eff} is the effective temperature at that time. Plotted points are the average of up to four individual measurements, and the error bars reflect statistical uncertainties. The dashed line shows the predicted variation in the rates calculated from the theoretical model discussed in the text.

10^6–10^7 atoms into our trap at densities of 10^9–10^{10} atoms/cm^3 and temperatures of ~ 100 μK. After loading the trap for approximately 1 s, we compress the trap by increasing the field gradient to 60 mT/m for $\sim$10–20 ms, transiently obtaining desities on the order of 10^{11} cm^{-3}.

After compression, we release the trap by turning off the MOT laser and magnetic fields. The compressed MOT shows significant variations in density across its profile, so we allow 4 ms of free expansion before imaging the cloud, to ensure smooth Gaussian profiles for the density extraction. The ionization rate is measured by counting the ions detected by a channel electron multiplier in a 0.5-ms window beginning 4 ms after the release of the trap. Images of the cloud are taken both before and after the ion count data are taken, to correct for slow changes in the MOT characteristics, and ten measurements of N and n_o are averaged for each β extraction.

We measure the initial spatial extent of the cloud, and initial temperature T_o, by measuring the size of the cloud at two delays after release of the trap, and fitting the expansion to the form of Eq. (19) to extract the initial size and average velocity. From these measurements, we calculate the effective temperature T_{eff} for our sample after 4 ms of free expansion.

Figure 3 shows the results of our measurements for five different isotopes, plotted as a function of T_{eff}. To remove uncertainties associated with the detector efficiency, we take our previous measure of $\beta_{\mathrm{unpol}}^{(132)}=6(2)\times 10^{-11}$ cm^3/s [12] for the absolute magnitude of the rate coefficient, and consider the ratios

$$\zeta_{\mathrm{unpol}}=\frac{\beta_{\mathrm{unpol}}}{\langle\beta_{\mathrm{unpol}}^{(132)}\rangle} \tag{24}$$

of the measured β_{unpol} for each isotope to the average of the measured rate coefficients for ^{132}Xe. Plotted points are the average of up to four measurements of ζ_{unpol} with similar values of T_{eff}, and the error bars reflect statistical uncertainties in both the measurements of β_{unpol} for each isotope and the average value of $\beta_{\mathrm{unpol}}^{(132)}$.

The dashed line shows the predicted variation in $\beta_{\mathrm{unpol}}^{(\mathrm{boson})}$ calculated using the simple model of Sec. II, scaled to $\beta_{\mathrm{unpol}}^{(\mathrm{boson})}=1$ at $T_{\mathrm{eff}}=60$ μK. The total predicted variation over the range of interest is $\sim$10%, which is less than the uncertainty in the measurement of ζ_{unpol}. The data are essentially constant over this range of temperatures.

The measured values of ζ_{unpol} are identical within the experimental uncertainties, consistent with our simple picture of a universal rate coefficient, independent of the isotope, for the strong inelastic ionization process (Sec. II). The average of the values of $\zeta_{\mathrm{unpol}}^{(136)}$ is 0.82(11) [25], and all measurements of $\zeta_{\mathrm{unpol}}^{(136)}$ are less than 1, which may indicate a real reduction in the collision rate for ^{136}Xe (which complex potential calculations show to be possible for extreme values of the scattering length [23]). However, the uncertainties in these measurements overlap the values for $\zeta_{\mathrm{unpol}}^{(132)}$, preventing us from definitively stating that the collision rate is lower for ^{136}Xe.

V. SPIN-POLARIZED COLLISION RATES

The MOT loading and compression sequence for the measurement of spin-polarized collision rates is identical to that for the measurement of unpolarized rates. Following the MOT compression, we turn off the MOT and slowing lasers and replace the quadrupole MOT field with a small, uniform magnetic field ($B_z\sim 0.1$ mT), by changing the current in our MOT coils. This field establishes a definite axis of quantization, and is maintained for the duration of the experiment. We minimize stray fields transverse to B_z by minimizing the temperature of atoms from a $\sigma^+-\sigma^-$ optical molasses, measured from the time-of-flight (TOF) distributions of atoms detected on a micro-channel plate (MCP) mounted 15 cm below the MOT.

We allow 0.5 ms for the field to reach steady state, then apply a 0.5-ms pulse of σ^+-polarized light tuned to the 882 nm $6s[3/2]_2\rightarrow 6p[5/2]_3$ laser cooling transition to optically pump the atoms into the $m_J=2$ magnetic sublevel of the $6s[3/2]_2$ state. The pumping beam is aligned with the field B_z, and retroreflected to minimize the effect of light forces on the atomic cloud.

We measure the spin polarization of the sample in the same manner as Ref. [29], by applying a pulse of light tuned to the 905-nm ''quench'' transition to the $6p[5/2]_2$ state, which rapidly decays (via the $6s[3/2]_1$ state, with 60% probability) to the ground state, emitting a vacuum ultraviolet (VUV) photon which we detect with the MCP. The ''quench'' beam is collinear with the optical pumping beam, and the σ^+ and σ^- circular polarizations of both quench and pumping beams are produced with a Fresnel rhomb.

As this ''quench'' excitation is a $J=2\rightarrow J'=2$ transition, atoms in the $m_J=2$ state cannot absorb σ^+-polarized light, and thus will not produce VUV photons. The ratio of VUV photons produced by a σ^--polarized pulse (which is readily absorbed) to those produced by a σ^+ pulse is a sensitive

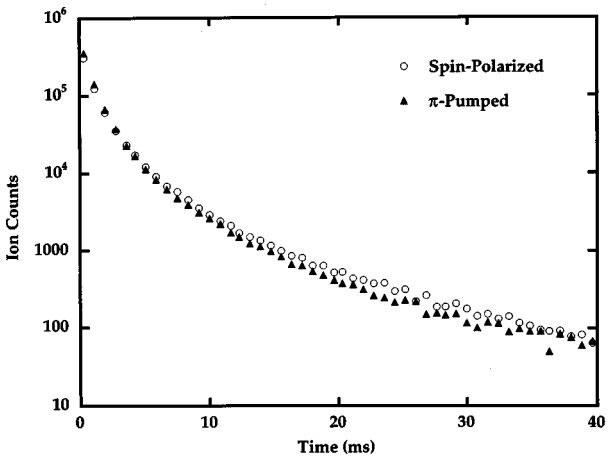

FIG. 4. Measured ionization rate as a function of time during ballistic expansion of the MOT. Plotted points are the sum of 1000 expansions for a sample of ^{132}Xe. Circles are data for a spin-polarized sample, triangles for a sample pumped with π-polarized light.

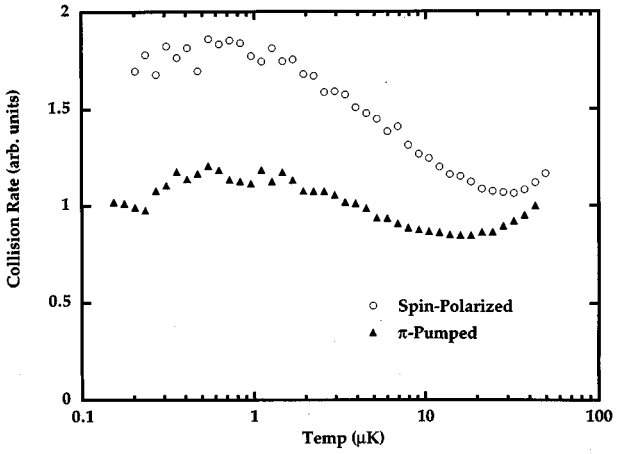

FIG. 5. Rate coefficients β extracted from the data of Fig. 4 as a function of the effective collision temperature $T_{\rm eff}$. Circles are data for a spin-polarized sample, triangles for a sample pumped with π-polarized light.

measure of the degree of polarization of the sample.

We typically find $\sigma^-:\sigma^+$ VUV count ratios of 10:1 or better, indicating that at least 90% of the atoms have been pumped into the $m_J=2$ sublevel. The quench pulse is applied in a 2-ms window 20 ms after release of the trap, and the polarization has been measured to be maintained for at least 40 ms after the optical pumping pulse.

All measurements with spin-polarized samples of the two fermionic isotopes are made without a repumping laser, leading to a greater uncertainty in the quality of the optical pumping. Measured ratios of VUV counts for σ^-/σ^+ polarizations are still 10:1 or better, but the VUV signal is partially masked by a large background of counts from atoms detected at the MCP which have been lost from the MOT by being pumped into the $F=\frac{3}{2}$ hyperfine level of ^{129}Xe, (or the $F=\frac{5}{2}$ for ^{131}Xe). We still expect polarizations of near 90% for these samples.

After optical pumping, the atoms are allowed to expand ballistically, and the rate of ion production is measured with a channel electron multiplier and multichannel scaler, which produces a histogram of ion production vs time. Figure 4 shows the sum of the ion counts detected during 1000 such expansions for a sample of ^{132}Xe.

The dramatic decrease in ionization seen in Fig. 4 is due to the decrease in the density of the sample as the cloud expands. From Eq. (23), we know that $R_i \approx \beta n N$, and if we assume a constant number of atoms (which is reasonable for the short expansions considered here), the density is approximately

$$n(t) \approx \frac{N}{(x_{\rm eff}(t))^3} = \frac{N}{\left[x_o^2\left(1+\frac{v_o^2 t^2}{x_o^2}\right)\right]^{3/2}}, \qquad (25)$$

where $x_{\rm eff}(t)$ is the rms width of the atomic density distribution at time t, from Eq. (19).

We calculate $x_{\rm eff}(t)$ using experimentally determined values of x_o and v_o, and also extract $T_{\rm eff}(t)$. We measure T_o and N from Gaussian fits to the TOF signals collected on the MCP, and correct N to account for the loss of atoms whose transverse velocities are large enough to cause them to miss the MCP. We extract x_o by measuring the size of the atom cloud at six different delays after release of the MOT, and extrapolating the expansion back to $t=0$. The two widths measured from two-dimensional Gaussian fits to our absorptive images of the MOT are averaged to give a single ''effective'' x_o. We divide the ion count data of Fig. 4 by $Nn(t)=N^2/x_{\rm eff}(t)^3$ to obtain $\beta(t)$, and thus $\beta(T_{\rm eff})$.

The ion detector used for these measurements is mounted ~ 6 cm above the MOT, and as the atom cloud falls under the influence of gravity, it will eventually reach a point where the electric field from the detector is no longer sufficient to attract and detect ions created in the cloud, which would produce an apparent decrease in the measured $\beta(t)$. We measure the ion production over 163 ms of ballistic expansion, and observe smoothly varying signals for the first ~ 80 ms, at which point the signal rapidly drops to zero. At this time, the cloud has fallen approximately 3 cm, and ions created at that point are most likely drawn into the MCP, and lost to our ion detector. We extract collision rates only from the first 40 ms of data, during which time the cloud has fallen only 0.8 cm, and we expect no significant variation in our detection efficiency.

Figure 5 shows the rate coefficient $\beta(T_{\rm eff})$ extracted from the data of Fig. 4. Circles show $\beta_{\rm pol}^{(132)}$ for a spin-polarized sample of ^{132}Xe. To account for residual light pressure forces from the pumping beam, which may affect the measurement of N by causing some atoms to miss the MCP detector, we compare this to $\beta_{\rm lin}^{(132)}$ (triangles), the rate coefficient for a sample optically pumped with π-polarized light. This produces a known distribution of m_J states (although most likely uniform, the exact distribution of states produced by the MOT is not well known), and theoretically is expected to differ from $\beta_{\rm unpol}^{(132)}$ by less than 7% over the temperature range of interest. Experimentally, $\beta_{\rm lin}^{(132)}$ and $\beta_{\rm unpol}^{(132)}$ have been

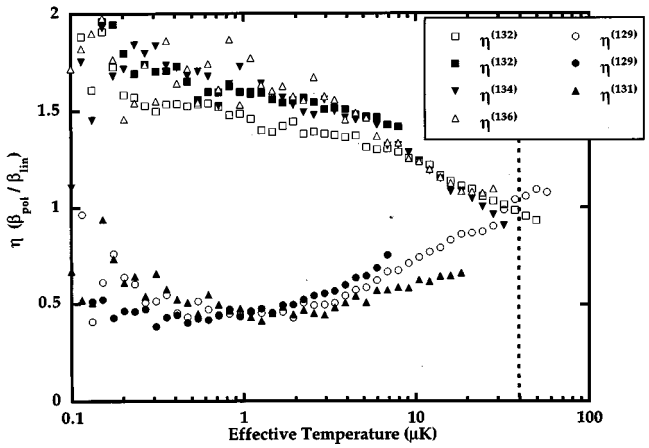

FIG. 6. Ratios $\eta(T)=\beta_{\rm pol}(T)/\beta_{\rm lin}(T)$ for three bosonic (^{132}Xe, ^{134}Xe, and ^{136}Xe) and two fermionic (^{129}Xe and ^{131}Xe) isotopes as a function of the effective collision temperature $T_{\rm eff}$. Filled boxes (circles) for ^{132}Xe (^{129}Xe) show data for samples with a lower initial temperature ($T_o\sim 20$ μK, instead of $T_o\sim 100$ μK). Plotted points are the weighted average of data from several expansions. The clear difference between spin species below the *p*-wave centrifugal barrier (dotted line) is the result of the quantum statistical effects discussed in the text.

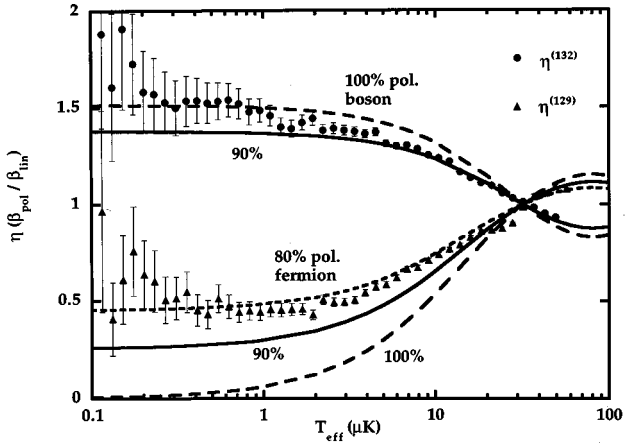

FIG. 7. Ratios $\eta(T)$ for ^{132}Xe (circles) and ^{129}Xe (triangles), compared to theoretical models. Solid lines represent calculations of $\eta(T)$ for samples with 90% polarization, dashed lines are for polarizations of 100%. The short-dashed line is calculated for an 80% polarized sample of ^{129}Xe. Error bars represent statistical uncertainties.

measured to be identical to within experimental uncertainties. The rapid variation of $\beta(T_{\rm eff})$ at high temperatures is due to small errors in the values of x_o and v_o used in the extraction, and does not reflect a real variation of β.

To correct for these systematic effects, and remove questions of detector efficiencies, we consider the ratio

$$\eta(T_{\rm eff})=\frac{\beta_{\rm pol}(T_{\rm eff})}{\beta_{\rm lin}(T_{\rm eff})} \tag{26}$$

of rate coefficients for polarized samples to linearly pumped samples when comparing the various isotopes. These ratios are plotted in Fig. 6 for the same five isotopes considered in Sec. IV (^{132}Xe, ^{134}Xe, ^{136}Xe, ^{129}Xe, and ^{131}Xe). Rates have been measured both for samples starting at normal MOT temperatures ($T_o\approx 100$ μK) and for samples with lower starting temperatures ($T_o\approx 20$ μK), obtained by adding 5 ms of cooling in σ^+-σ^- optical molasses between the compressed MOT and optical pumping phases. The plotted curves are the weighted average of data for several expansions. Differences between values of η for the same isotope reflect uncertainties in measurements of N, x_o, and T_o, and variation in the degree of polarization of the samples.

The data show a dramatic difference between the two spin species. For all three bosonic isotopes, $\eta(T_{\rm eff})$ increases from ~ 1 at the *p*-wave centrifugal barrier (39 μK), and approaches a value of $\eta(T_{\rm eff})\sim 1.6$ below 1 μK. For the two fermionic isotopes, $\eta(T_{\rm eff})$ decreases below the *p*-wave barrier, and is slightly less than 0.5 at effective temperatures below 1 μK. This is unambiguous evidence of the quantum-statistical effects described in Sec. II B.

Data for ^{132}Xe and ^{129}Xe are compared to our simple theoretical model in Fig. 7. The data for ^{132}Xe match well to the theoretical $\eta(T)$ for the ratio for a sample with 90% or better spin polarization, including $\eta(T)<1$ at temperatures above the *p*-wave barrier. The measured $\eta^{(129)}(T_{\rm eff})$ are consistent with calculations for slightly lower polarizations (80–90 %). This may be due to atoms which have been optically pumped into the $F=\frac{3}{2}$ hyperfine level (although a simple estimate suggests that this should not be a significant effect), or it may simply reflect less efficient optical pumping for these isotopes, which is consistent with the measured polarizations.

The calculations shown in Fig. 7 are carried out assuming no change in the collision rate coefficients due to the spin-conservation effects discussed in Sec. II C. The good agreement between this simple theory and our data allows us to place limits on the magnitude of any spin-conservation effects (Sec. II C). We calculate theoretical rate coefficients assuming a spin polarization of between 90% and 100% for the sample, and allowing the rate coefficient for collisions between two atoms both in the $|J=2, m_J=\pm 2\rangle$ internal states to vary with respect to that for atoms in any other combination of internal states. We find that good agreement between theory and experiment can be maintained only for very small ($\sim 5\%$) changes in the rate coefficient for two $|2,2\rangle$ atoms.

This suggests that the collision rates are entirely independent of the internal m_J states of the colliding atoms, and that the spin-conservation effects seen in He* are not present in xenon. We interpret this result as being a consequence of the anisotropic interactions described in Sec. II C and Ref. [17], which shows theoretically that such interactions can even produce a substantial increase in the spin-polarized collision rates for Xe*.

VI. CONCLUSIONS

We have measured collisional rate coefficients for five xenon isotopes, three bosons and two fermions, and found that for unpolarized samples above the *p*-wave centrifugal barrier, the rates for all isotopes are identical to within 20%.

We have used the ''expansion cooling'' effect to measure these rates at very low collision temperatures, and find dramatic differences between spin-polarized samples of fermions and bosons at temperatures below the *p*-wave barrier. We see that the ratio of polarized to unpolarized rate coefficients increases by more than 60% for bosonic isotopes, while the ratio for fermions decreases by more than a factor of 2, reflecting the fact that quantum statistics forbids *s*-wave collisions for fermions. These results are well described by the predictions of a simple theoretical model of transmission and quantum reflection off long-range interatomic potentials.

Our results also show that, for the Xe* system, the spin-conservation effects seen in He* and expected in Ne* are completely absent. To within experimental uncertainties, we find no dependence of the collisional rate coefficient on the internal states of the colliding atoms. We interpret this result as evidence of anisotropic interactions which reorient the internal atomic states and lift the spin-conservation restriction. These interactions should be much stronger in Xe* (and Kr*, where similar results have been observed [20]) than in the lighter metastables, but experimental studies of these rates in the lighter rare-gas metastables are needed, especially given the importance of spin-conservation effects to experimental hopes for Bose-Einstein condensation in these systems. These experiments could also be extended to samples with higher degrees of spin polarization than seen in the present work, by working with samples in magnetic traps.

ACKNOWLEDGMENTS

We thank J. Lawall, S. D. Bergeson, and S. Kulin for valuable experimental assistance, and E. J. D. Vredenbregt and C. J. Williams for helpful discussions. This work was supported in part by the U. S. Office of Naval Research. C. O. was supported by a Joint NIST/ UMCP Fellowshp in AMO Physics. U. S. acknowledges funding from the Alexander von Humboldt Foundation.

[1] J. Weiner, V. S. Bagnato, S. Zilio, and P. S. Julienne, Rev. Mod. Phys. (to be published); P. S. Julienne, A. M. Smith, and K. Burnett, Adv. At., Mol. Opt. Phys. **30**, 41 (1993); T. Walker and P. Feng, *ibid.* **34**, 125 (1994); J. Weiner *ibid.* **35**, 45 (1995).

[2] K. Gibble and S. Chu, Phys. Rev. Lett. **70**, 1771 (1993).

[3] W. Ketterle and N. J. Van Druten, Adv. At., Mol., Opt. Phys. **37**, 181 (1996).

[4] R. J. Dodd, M. Edwards, C. J. Williams, C. W. Clark, M. J. Holland, P. A. Ruprecht, and K. Burnett, Phys. Rev. A **54**, 661 (1996).

[5] J. Söding, D. Guéry-Odelin, P. Desbiolles, G. Ferrari, and J. Dalibard, Phys. Rev. Lett. **80**, 1869 (1998).

[6] P. D. Lett, P. S. Julienne, and W. D. Phillips, Annu. Rev. Phys. Chem. **46**, 423 (1996).

[7] P. S. Julienne, and F. H. Mies, J. Opt. Soc. Am. B **6**, 2257 (1989).

[8] K.-A. Suominen, J. Phys. B **29**, 5981 (1996).

[9] M. R. Doery, E. J. D. Vredenbregt, J. G. C. Tempelaars, H. C. W. Beijerinck, and B. J. Verhaar, Phys. Rev. A **57**, 3603 (1998).

[10] J. Lawall, C. Orzel, and S. L. Rolston, Phys. Rev. Lett. **80**, 480 (1998).

[11] H. Kunugita, T. Ido, and F. Shimizu, Phys. Rev. Lett. **79**, 621 (1997).

[12] M. Walhout, U. Sterr, C. Orzel, M. Hoogerland, and S. L. Rolston, Phys. Rev. Lett. **74**, 506 (1995).

[13] K.-A. Suominen, K. Burnett, P. S. Julienne, M. Walhout, U. Sterr, C. Orzel, M. Hoogerland, and S. L. Rolston, Phys. Rev. A **53**, 1678 (1996).

[14] H. Katori and F. Shimizu, Phys. Rev. Lett. **73**, 2555 (1994).

[15] H. C. Mastwijk, J. W. Thomsen, P. van der Straten, and A. Niehaus, Phys. Rev. Lett. **80**, 5516 (1998).

[16] C. Orzel, S. D. Bergeson, S. Kulin, and S. L. Rolston, Phys. Rev. Lett. **80**, 5093 (1998).

[17] M. R. Doery, E. J. D. Vredenbregt, S. S. Op de Beek, H. C. W. Beijerinck, and B. J. Verhaar, Phys. Rev. A **58**, 3673 (1998).

[18] G. V. Shlyapnikov, J. T. M. Walraven, U. M. Rahmanov, and M. W. Reynolds, Phys. Rev. Lett. **73**, 3247 (1994); P. O. Fedichev, M. W. Reynolds, U. M. Rahmanov, and G. V. Shlyapnikov, Phys. Rev. A **53**, 1447 (1996).

[19] W. Rooijakkers, W. Hogervorst, and W. Vassen, Opt. Commun. **135**, 149 (1997).

[20] H. Katori, H. Kunugita, and T. Ido, Phys. Rev. A **52**, R4324 (1995).

[21] Other terms of the form $\pm C_n/R^n$ may contribute to the potential, most notably the $\pm C_5/R^5$ quadrupole-quadrupole potential. This term is significantly smaller than the van der Waals term, and it and higher-order terms may be neglected in discussions of centrifugal barriers.

[22] These arguments apply to associative ionization as well. However, recent work [16] has shown that the associative ionization rate for collisions between xenon atoms in the $6s[3/2]_2$ state is negligible. We therefore refer only to Penning ionization for the remainder of this paper.

[23] C. J. Williams (private communication).

[24] D. Vrinceanu, M. Marinescu, and M. R. Flannery, Bull. Am. Phys. Soc. **43**, 1304 (1998).

[25] All quoted uncertainties are 1-standard deviation values.

[26] For simplicity, we refer to $|J,m_J\rangle$ states for both bosons and fermions. The fermionic isotopes are more properly described by $|F,m_F\rangle$ hyperfine states (the bosonic isotopes have no nuclear spin, and thus no hyperfine structure). Explicitly considering the effects of nuclear spin adds a numerical factor to the equations of Sec. II B, but does not change the conclusions.

[27] J. C. Hill, L. L. Hatfield, N. D. Stockwell, and G. K. Walters, Phys. Rev. A **5**, 189 (1972).

[28] M. Walhout, H. J. L. Megens, A. Witte, and S. L. Rolston, Phys. Rev. A **48**, R879 (1993).

[29] M. Walhout, A. Witte, and S. L. Rolston, Phys. Rev. Lett. **72**, 2843 (1994).